The role of hydrothermal conditions in determining 1D TiO 2 nanomaterials bandgap energies and crystal phases

Tao Peng, Srimanta Ray, Sathyanarayanan Sevilimedu Veeravalli, Jerald A Lalman, Farzaneh Arefi-Khonsari

The role of hydrothermal conditions in determining 1D TiO_2 nanomaterials bandgap energies and crystal phases

Tao Peng[a,b], Srimanta Ray[c], Sathyanarayanan Sevilimedu Veeravalli[d], Jerald A. Lalman[a,#], Farzaneh Arefi-Khonsari[b, ##]

[a] Department of Civil and Environmental Engineering, University of Windsor, 401 Sunset Ave., Windsor, Ontario N9B 3P4, Canada
[b] *Sorbonne Université, CNRS, Laboratoire Interfaces et Systèmes Electrochimiques, LISE, 75005 Paris, France*
[c] Department of Chemical Engineering, National Institute of Technology Agartala, Tripura, India, 799055
[d] Civil Engineering, Kansas State University, Manhattan, KS 66506, USA

#Jerald A. Lalman, Voice: +1-519-253-3000 ext. 2519; Fax + 1-519-971-3686; Email: lalman@uwindsor.ca
##Farzaneh Arefi-Khonsari, Voice: +33-144276815; Fax: +33-144276813; Email: farzaneh.arefi@upmc.fr

Graphical abstract

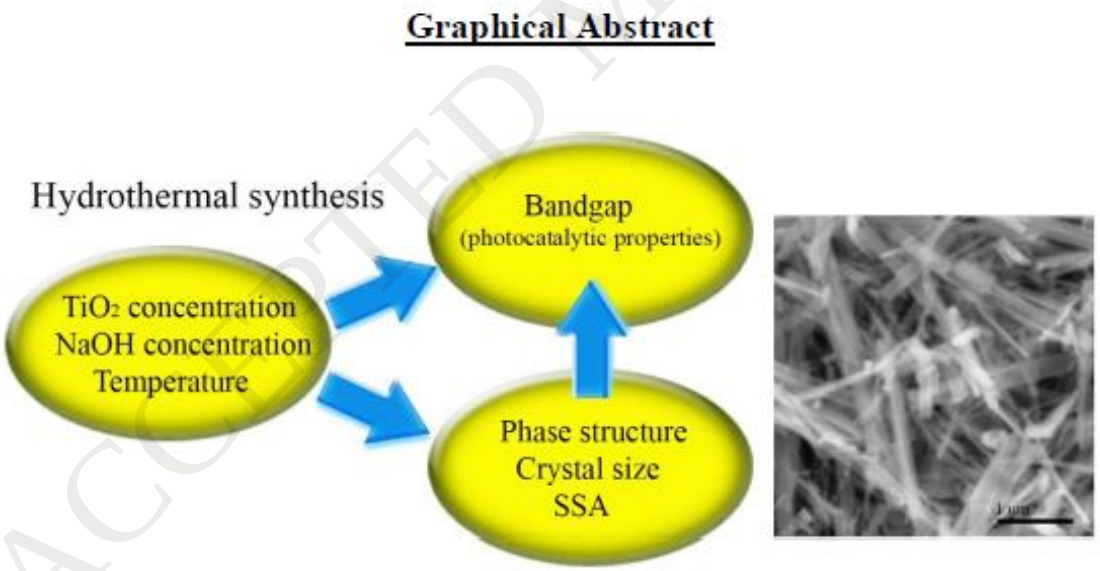

HIGHLIGHTS

- Application of hydrothermal method for 1D TiO2 synthesis.
- Varying hydrothermal synthesis conditions on 1D TiO2 crystal phase, size and SSA.
- Effects on crystal phase, size and SSA on bandgap.

Abstract

One-dimensional TiO_2 nanostructure synthesized using a hydrothermal method showed significant differences in the bandgap energies and crystal phase properties under different synthesis conditions. The objectives of this study were to evaluate the effect of the hydrothermal reaction conditions on the bandgap energy and to optimize the reaction conditions using a 3-factor 3-level Box Behnken design. The factors investigated include temperature, NaOH concentration and TiO_2 concentration (BBD). A quadratic response surface model predicted optimum conditions for the maximum and minimum bandgap energy. The BBD analysis and other statistical tools provided evidence showing the temperature and NaOH concentration significantly affected the 1D TiO_2 bandgap energy. Pure anatase was associated with a higher bandgap energy, whereas the biphasic anatase-rutile and anatase-TiO_2-B phases were linked with decreasing the bandgap energy. In addition, the crystal size and specific surface area (SSA) impact on the bandgap energy was due to the size quantization effect.

Key words: One-dimensional TiO_2; Bandgap; Hydrothermal synthesis; Anatase; TiO_2-B.

1. Introduction

The discovery of photo-electrochemical splitting of water on n-TiO_2 electrodes in 1972 [1] triggered much attention in examining the photoelectrolysis of water to hydrogen (H_2) and oxygen (O_2). Other applications include employing n-TiO_2 in wet solar cells [2] and for the photodegradation of hazardous organics pollutants into carbon dioxide plus water [3-6]. One-dimensional (1D) TiO_2 nanomaterials have shown significant potential in these applications because of their high electron mobility, large specific surface area (SSA) and high mechanical

strength [7-11]. Among the different approaches used to synthesize 1D TiO_2, the alkaline hydrothermal method is a relatively easy process for producing 1D TiO_2 with varied bandgap energies [7,8,10-19]. Bandgap energies are crucial in determining the 1D TiO_2 photocatalytic efficiency [7].

The band gap is significantly affected by factors such as phase structure, temperature and crystal size. Phase structure is a major factor affecting 1D TiO_2 bandgap. TiO_2 has an optical bandgap value for different crystal phases. For TiO_2, the band gap is 3.2 eV for anatase, 3.0 eV for rutile, 3.1 eV for brookite and 3.2 eV for TiO_2-B [10,17,20]. Work by Bavykin et al. [8] has shown that during the alkaline hydrothermal process, TiO_2 precursors (anatase, rutile, TiO_2-B, brookite and amorphous) were reconstructed into 1D TiO_2 by producing and consecutively wrapping titanate nanosheets. Different crystal phase structures can be produced during hydrothermal processing [7,8,10-19]. Zhu et al. [14] claimed that the anatase phase was produced when using 15 M NaOH at a temperature between 20^{o}C and 200^{o}C for 48 hours. In other studies, Kou et al. [17] reported TiO_2-B nanotubes were obtained when the conditions were set by employing 10 M NaOH at 120^{o}C for 96-168 hours. In these studies, researchers used selected synthesis conditions to produce 1D TiO_2 structures with varied phase structures. An existing research gap which requires addressing is the assessment of different synthesis conditions on the phase structure and bandgap energy for 1D TiO_2 nanostructures.

TiO_2 band structure changes is also affected by crystal size lower than that of the exciton in TiO_2 [21]. This observation, designated as the size quantization effect [10,21], causes the TiO_2 bandgap energy to shift to larger values or shorter wavelengths for decreasing crystal sizes [10]. Many studies have shown 1D TiO_2 diameters ranging from 5 nm to 200 nm can be controlled using selected hydrothermal temperatures and suitable TiO_2:NaOH molar ratios [8,12,13].

Bavykin et al. [8] reported the average 1D TiO_2 diameter increased with an increase in the temperature from 120°C to 150°C and with increasing the TiO_2:NaOH weight ratio. Adjusting the temperature and NaOH:TiO_2 weight ratio are expected to impact the crystal size and subsequently, the bandgap energy based on the size quantization effect [10].

The lack of research data describing the role of different hydrothermal synthesis process parameters on the 1D TiO_2 phase structure and its bandgap energy is the motivating factor for conducting this study. One objective was to employ a Box-Behnken design (BBD) to statistically model the influence of the hydrothermal synthesis factors on the 1D TiO_2 bandgap energy. The three hydrothermal synthesis factors under consideration included temperature, NaOH concentration and TiO_2 precursor concentration. Another objective was to evaluate the influence of hydrothermal synthesis factors on the 1D TiO_2 phase structure, crystal size and SSA.

2. Experimental

2.1. Preparation of 1D nanometric TiO_2 photocatalyst

1D TiO_2 samples were prepared using the alkaline hydrothermal method [8,10-17,22]. In general, TiO_2 nanoparticles (Aeroxide TiO_2 P25, Evonik Corporation, Parsippany, New Jersey) were dispersed in 70 mL of a NaOH solution. The TiO_2 and the NaOH concentrations are shown in Table 1. The resulting suspension was transferred into a 100-mL Teflon lined stainless-steel autoclave. The autoclave was maintained at a desired temperature (Table 1) for 120 h and subsequently, cooled to room temperature. Next, the suspension was centrifuged to obtain a white precipitate. The precipitate was washed with 1L of 0.1 M HCl for 24 h at room temperature. The white precipitate was repeatedly washed (5 times) with deionized water. The washed mixture was centrifuged after each washig with deionized water. Finally, the white

precipitate was calcined at 400°C for 2 hours to produce 1D TiO_2. The selected experimental levels were based on previous studies (Table 1) [8].

2.2. Characterization studies

The 1D TiO_2 morphology was examined using scanning electron microscopy (SEM) (JEOL, Japan) and high resolution transmission electron microscopy (HRTEM) (300kV, JEOL 3010, Japan). X-ray diffraction (XRD) analysis of the samples was conducted using an X-ray diffractometer (Rigaku, MI) equipped with Cu K_∂ radiation source. UV-Vis spectra analysis was performed using a Cary 300 UV-Visible (Agilent Technologies, Santa Clara, CA). The wavelength accuracy and resolution for the Cary 300 UV-Visible were $\pm$0.04 nm (at 486 nm) and $\leqslant$0.193 nm, respectively. The bandgap energy response was calculated based on diffuse reflectance UV-vis spectroscopy studies. The diffuse reflectance spectra were converted into a corresponding absorption spectra using the modified Kubelka Munk function $(F(R)E)^{1/2}$ [23]. Frequent use of diffuse reflectance UV-vis spectroscopy to determine the bandgap energy in solid materials is highly justified based on past research [23]. The bandgap energy (E_g) for each experiment is shown in Table 2. The photoluminescence spectra were conducted at room temperature using a Varian Cary Eclipse Fluorescence Spectrophotometer (Mississauga, ON). Nitrogen adsorption–desorption isotherms were determined at 77K with a Micromeritics ASAP 2020 Brunauer–Emmett–Teller (BET) analyzer (Micromeritics Instrument, Norcross, GA).

2.3. Experimental design, optimization study and statistical analysis

A three factor three level BBD was constructed with three central points to determine the hydrothermal synthesis factors for evaluating the bandgap energy. The BBD is unique because it

is rotatable and does not comprise an embedded factorial or fractional factorial design. The BBD experimental conditions were selected at the midpoints of edges of the space and at the center.

Each experimental factor was varied at a low level (designated as -1), a central level (designated as 0) and a high level (designated as +1) (Table 1). The method is constructed using 12 experimental points (#1 to #12) plus three central points (#13 to #15) and each condition under triplicate conditions (Table 2). The three central point experiments, designated as #13, #14 and #15 under the same conditions, were performed to evaluate the magnitude of error in the experimental analysis. The experimental factors and bandgap energy (response variable) were modeled using Minitab (Minitab Inc., State College, PA) to fit a full quadratic equation (equation (1)):

$$E_g = a_0 + \sum_{i=1}^{3} a_i X_i + \sum_{i=1}^{3} a_{ii} X_i^2 + \sum_{i=1}^{3} \sum_{i<j=2}^{3} a_{ij} X_i X_j \quad (1)$$

where X_i's are input variables which influence the response variable E_g, a_o is an offset term, a_i is the i^{th} linear coefficient, a_{ii} is the quadratic coefficient, and a_{ij} is the ij^{th} interaction coefficient. The X_i correspond to the experimental factors (X_1 = temperature, X_2 = NaOH concentration, X_3 = TiO_2 concentration) (Table 2).

An analysis of variance (ANOVA) was performed using the responses for each experimental condition (#1 to #15) (Table 2). The coefficient values for the full quadratic model were calculated using a multiple regression analysis. Only significant terms with p values < 0.05 were included into the final model. A normal distribution plot together with the Anderson-Darling (AD) [24] statistic was used to determine the deviation of the residuals from a normal

distribution. The D-optimality analysis [25] was performed to obtain optimal conditions for the three factors under consideration (maximize and minimize the bandgap energy E_g).

3. Results and discussion

3.1. Morphology

SEM images for selected 1D TiO_2 samples are shown in Figure 1. 1D TiO_2 samples (nanorods and nanowires) synthesized at different hydrothermal conditions which were randomly distributed showed significant differences in the crystal sizes. The SEM image for sample #1 (120^{o}C, 5 M and 43 g L^{-1}) indicate a mixture of nanorods and nanowires with length of approximately 100 nm. Nanowire morphology with length up to 2 um was detected in sample #6 (190^{o}C, 10 M and 14 g L^{-1}). Lower temperature and NaOH concentration were associated with smaller diameter and crystal size (Sample #1). However, higher temperature and NaOH concentration were linked to larger diameter and crystal size (Sample #6). The SEM images indicate the hydrothermal synthesis factors significantly impacted the 1D TiO_2 diameter and crystal size (further discussed in Section 3.3.6 Crystal size and BET SSA). During hydrothermal process, NaOH reacted with TiO_2 crystallites and produced free TiO_6 octahedron by cleaving the Ti-O-Ti bonds of TiO_2 precursor [26,27]. The TiO_6 octahedron was subsequently assembled into lamellar structures via the formation of hydroxyl bridges between the Ti atoms [8,27,28]. Next, 1D TiO_2 (nanotubes, nanorods and nanowires) was produced by scrolling or growing the lamellar structures [8,28]. The driving force for converting lamellar structures scrolling into nanotubes or growing into nanorods or nanowires is attributed to the reducing the high surface energy of the nanosheets which was caused by the saturated the dangling bonds on the nanosheets [26].

3.2. Bandgap energy (eV)

Diffuse reflectance UV-visible spectroscopy (DRS) was employed to examine the optical response of the starting material TiO_2 nanoparticles and the resulting 1D TiO_2 (Figure 2a). A wide optical absorption below a critical value of approximately 410 nm was observed in both samples [29]. This broad band assignment is attributed to the band-band electron transition of the TiO_2 nanocrystals based on its band gap energy [29,30]. A red-shift and enhanced light absorption between 300 to 400 nm was observed for the 1D TiO_2 sample #1 when compared to TiO_2 nanoparticles. The diffuse reflectance spectra was converted into a corresponding absorption spectra (Figure 2b) by plotting $(F(R)*E)^{1/2}$ versus E (where $F(R) = a_{Km}$ is the Kubelka Munk function [23] and E is the photon energy). Extrapolating the straight line portion of the UV-visible spectra to $(F(R)*E)^{1/2}=0$ was used to determine the bandgap energy. A 3.07±0.01eV value for the 1D TiO_2 sample #1 was less than that for the TiO_2 nanoparticles bandgap of 3.28±0.01eV. In this study, the bandgap energies for the 15 BBD samples (ranging from 3.07±0.01 eV to 3.297±0.005 eV) are shown in Table 2. The observed change in the bandgap energy for the different samples was due to changes in crystal phase and size under the different hydrothermal conditions.

3.3. Analysis of the experimental design

3.3.1. Impacts of factor variables on the bandgap energy

The bandgap energy for all the 1D TiO_2 samples are shown in Table 2 and the main effect of 3 hydrothermal synthesis factors on the bandgap energy is shown in Figure 3. A mid-level temperature set at 150^{o}C as well as the mid-level NaOH concentration of 10 M were closely

linked with increasing the bandgap energy. Either increasing or decreasing temperatures (NaOH concentrations) resulted in decreasing the bandgap energy. An opposite trend was observed for changes in the TiO_2 concentration. The mid-level TiO_2 concentration was related to a decrease in the bandgap energy. Interaction plots at all level factor categories (Figure 3b) indicate a similar pattern as that shown in the main effect plot. An increasing bandgap energy value was observed at a mid-level temperature of 150^{o}C and a mid-level 10 M NaOH concentration.

3.3.2. Model fitting using ANOVA

An ANOVA was employed to evaluate the significance of the full quadratic model and to determine the significance and adequacy of the model. The ANOVA result (Table 3) for the bandgap energy (E_g) response shows that the model is statistically significant with a p-value less than 0.05. The model F-value of 44 which was greater than the F-critical value of 2.01 at an α value = 0.05 indicate the full quadratic model was significant [25,31-33]. Note, the terms with p-values < 0.05 are statistically significant whereas terms with a p-value > 0.05 are insignificant. TiO_2 concentration (g L^{-1}), NaOH concentration (M) x NaOH concentration (M) and TiO_2 concentration (g L^{-1}) x TiO_2 concentration (g L^{-1}) with p-values more than 0.05 are statistically insignificant indicate these variables did not affect the full quadratic model [25,31-33].

A full quadratic model can be simplified using a stepwise procedure such as a backwards elimination method. Other stepwise procedures include forward selection and stepwise regression. The selected backwards elimination method in this study is advantageous because of considerable predictability. The method is employed to delete statistically insignificant terms with p values > 0.05 in the full model [25]. The refined model (equation 2) with an F-value of 6.97 (> the critical level (6.7, $p < 0.00$)) is statistical significant.

$$E_g = 3.2742 - 0.01648X_1 - 0.0111X_2 - 0.01882X_1X_2 + 0.00881X_1X_3 + 0.1171X_2X_3 - 0.02798X_1^2 \quad (2)$$

where E_g is the bandgap energy (eV), X_1, X_2 and X_3 represent temperature (^oC), NaOH concentration (M) and TiO_2 concentration (g L^{-1}), respectively.

3.3.3. Factor interaction plots

Describing the interactions between the experimental factors was based on data in the surface and contour plots. Interaction between temperature and NaOH concentration (Figure 4a and Figure 4b) suggests that a minimum bandgap (3.07±0.01 eV) was observed for the 1D TiO_2 sample synthesized at 120^{o}C and 5 M NaOH. The bandgap energy increased to approximate 3.297±0.005 eV when the temperature was increased to approximate 170^{o}C. However, high NaOH concentrations reaching up to 10 M and 15 M along with a relative high temperature set at 190^{o}C contributed to decreasing the bandgap energy (ranging from 3.20±0.01 to 3.23±0.01 eV). Interaction between temperature and TiO_2 concentration (Figure 4c and Figure 4d) is a strong indication that variations in the TiO_2 concentration under consideration did not affect the bandgap energy. However, the temperature alone affected the bandgap energy at all the TiO_2 concentrations under consideration. Relative high temperatures ($\geq 170^oC$) (Figure 4c and Figure 4d) were associated with decreasing the bandgap (3.20±0.01 to 3.27±0.01 eV). Interaction between NaOH and TiO_2 concentrations (Figure 4e and Figure 4f) confirmed that the TiO_2 concentration did not affect the bandgap energy and the phase structure. When the temperature was set at 150^{o}C (Figure 4c and Figure 4d), the bandgap energy varied between

3.27±0.01 to 3.297±0.005 eV along with variation in the TiO_2 concentration and NaOH concentration.

3.4.Response model verification, optimization and validation

The regression coefficient R^2 value for the bandgap energy model was 0.936. The R^2 value indicates the bandgap values predicted using the model correlated reasonably well with the experimental data. A scatter plot of the experimental values versus the predicted values calculated using the model equation illustrates a reasonable correlation at each level (Figure 5a). Evaluating the adequacy of fit between the model and the experimental data was conducted using the the Anderson-Darling (AD) statistic (Figure 5b) [34]. The AD statistic was 0.488 for the Eg model. This value which is less than the critical AD value of 0.735 for a sample size of 45 at a 5% level of significance suggest the residuals p-value of 0.213 (> the critical value of 0.05) was able to meet the normal distribution requirement.

The D-optimality was used to establish the region of maximum and minimum response (bandgap energy). Within the factor space under consideration, the D-optimality value can vary from 0 (completely undesirable) to 1 (completely desirable) using the numerical optimization function in the Minitab® software. Values for temperature, NaOH and TiO_2 concentrations at the maximum and minimum bandgap energy values were identified at the largest D-optimality index (Figure 6). A maximum bandgap energy of 3.31 eV was obtained at a D-optimality value of 0.874 under conditions set at 150^{o}C, 12 M NaOH and 14 g L^{-1} TiO_2. In comparison, a minimum bandgap energy of 3.05 eV was predicted at a D-optimality value of 0.854 at 120^{o}C, 5 M NaOH and 63 g L^{-1} TiO_2. Validating the model predicted maximum and minimum bandgap values under the optimized hydrothermal conditions revealed experimental maximum and minimum

bandgap energy of 3.305±0.004 eV and 3.044±0.002 eV, respectively. The experimental band gap values were slightly underestimated when compared to the values predicted by the model.

The accuracy of the model within the experimental factors under consideration was examined by conducting three additional experiments. The experimental results together with the predicted values were obtained by varying a single factor (Figure 7). The model predicted values were close to the experimental values for the temperature ranging from 120^{o}C to 190^{o}C (Figure 7a), although the model predicted bandgap values were slightly overestimated at 150^{o}C. For the NaOH concentration, the predicted values were comparable to the experimental points with a slight overestimate at 5 M NaOH and a slight underestimate at 15 M NaOH (Figure 7b). For the TiO_2 concentration, the model predicted values were comparable to the observed values with a slightly overestimate at 43 g L^{-1} TiO_2 (Figure 7c). Notably, the model predicted trend for varying each factor were close to the experimental observations.

3.5. Phase structure analysis

Evaluating the impact of the crystal phase structure on the bandgap energy was performed using XRD. The XRD patterns (Figure 8a) for selected BBD samples #1, #2 and #6 and the phase structure for all the samples are listed in Table 4. The anatase [35], rutile [20,30] and TiO_2-B [17,36] phases were detected in selected samples with the anatase phase observed in all the 1D TiO_2 samples. Sample #2, #3, #5, #7, #9, #10, #11, #12, #13, #14 and #15 consisted of pure anatase with bandgap energy ranging from 3.26±0.01 to 3.297±0.005eV. The biphasic anatase-rutile structure dominated the 1D TiO_2 sample #1 while the biphasic anatase-TiO_2-B was dominant in sample #4, #6 and #8. This difference in phase change is also shown in Figure 4 illustrate the impact of the hydrothermal synthesis factors affecting the phase structure and

bandgap energy. Temperature and NaOH concentration were significant factors affecting the 1D TiO_2 phase structure. At a relative lower temperature (120^oC) and a low NaOH concentration (5 M), a bi-phasic anatase-rutile structure was observed in sample #1. Sample #1 was the only experimental design condition with the same biphasic anatase-rutile structure as TiO_2 NPs (P25) [30,37,38]. The relative low bandgap energy (3.07±0.01 eV) for the bi-phasic anatase-rutile structure is attributed to rutile which has a relative narrow bandgap energy of 3.0 eV [20,39]. Increasing the temperature and NaOH concentration resulted in the production of a pure anatase structure with a relative high bandgap energy value (3.26±0.01 - 3.297±0.005 eV). When the temperature was set at 190^oC with the NaOH concentration at 10 M or 15 M, the TiO_2-B phase (3.20 eV) was predominant in samples #4, #6 and #8 together with a small quantity of the anatase phase. The existence of TiO_2-B lowered the bandgap energy range from 3.20±0.01 to 3.23±0.01 eV, since TiO_2-B has a bandgap energy of 3.20 eV [17,40]. A few studies have shown existence of the TiO_2-B phase when using temperatures and a NaOH concentration of 150-190^oC and 10 M, respectively [18,40].

Photoluminescence studies (Figure 8b) for selected samples and the control (TiO_2 NPs) further demonstrated that the phase structure had a fundamental effect on the bandgap energy. All the samples showing a peak at 3.4 eV was due to the anatase fundamental band-to-band transition [41-43]. The tail from 3.1 to 3.4 eV in addition to the peak at 3.4 eV is assigned to the exciton trapped at shallow level defects for sample #15 [41,42]. However, the biphasic anatase-rutile (samples #1 and commercial TiO_2 NPs) and biphasic anatase-TiO_2-B (such as samples #4) showed a broader peak with a tail from 2.9 to 3.4 eV in addition to the anatase peak at 3.4 eV when compared to pure anatase (#15). This long tail is attributed to the lower band-to-band

transition of rutile and TiO_2-B crystal phase [44]. The band from 2.4 to 2.6 eV is due to the oxygen vacancies which behaved as the centers for indirect recombination [42].

3.6. Crystal size and BET SSA

The mean crystal sizes (L, nm) for sample #1-15 (Table 5) were calculated using Scherrer equation (Equation 3) and XRD data (data not shown).

$$L=K\lambda/\beta.\cos\theta \text{ [45]} \quad (3)$$

where K, λ and β represent the shape factor (0.89), the wavelength of XRD radiation (0.154 nm) and the half maximum of a full peak, respectively.

The main effect of hydrothermal synthesis factors on the mean crystal size are shown in Figure 9a. The synthesis temperature and NaOH concentration significantly affected the crystal size, whereas, the TiO_2 precursor concentration did not impact the crystal size. Decreasing crystal size was closely linked with lower temperatures and lower NaOH concentrations. Increasing the hydrothermal temperature from 120^{o}C to 190^{o}C or NaOH concentration from 5 M to 15 M resulted in an increase in mean 1D TiO_2 crystal size from 10 nm to 60 nm. The interaction plots (Figure 9b) indicate a similar pattern as shown in the main effect plot. This observation is consistent with work reported by Bavykin et al. [8]

The BET SSA for all the BBD samples, the main effects and interaction plots of the three hydrothermal synthesis factors on the mean BET SSA are shown in Table 5 and Figure 10, respectively. The data trend in Figure 10 for the BET SAA contrasts the trend for the mean crystal size data shown in Figure 9, since the high BET SSA was closely linked to the small

crystal size for the 1D TiO_2 nanostructure. Increasing the BET SSA was closely correlated with decreasing temperatures and decreasing NaOH concentration. The highest BET SSA was 181±5 $m^2\ g^{-1}$ for 1D TiO_2 sample #1 synthesized at 120°C, 5 M NaOH and 43 g L^{-1} while the lowest BET SSA was observed for sample #4 synthesized at 190°C, 15 M NaOH and 43 g L^{-1} TiO_2. The TiO_2 concentration did not impact the BET SSA. The interaction plots (Figure 10b) indicate a similar pattern as shown in the main effect plot. A larger BET SSA value was observed with decreasing temperatures as well as decreasing the NaOH concentration.

3.7. Effects of crystal size and SSA on 1D TiO_2 bandgap energy

Interaction between temperature and the NaOH concentration on bandgap energy, mean crystal size and BET SSA is shown in Figure 11. The trend for bandgap energy was relatively the same as that for BET SSA, whereas an opposite trend was observed for the mean crystal size. One exception observed at 120°C and 5 M NaOH was a biphasic anatase-rutile structure with the lowest bandgap energy of 3.07±0.01 eV. This exception is due to difference in the phase structure. For the 1D anatase TiO_2 samples synthesized at 150°C , the decrease in mean crystal size which was observed from 21 nm to 18 nm (an increase in BET SSA) resulted in increasing the bandgap energy from 3.26±0.01 eV to 3.297±0.005 eV. This bandgap increase is due to the size quantization effect [10,21]. Smaller crystal size was closely linked to a larger bandgap energy according to size quantization effect [10,21]. From the Figure 11, the mean bandgap energy, E (eV), is:

$$E = 3.4188 - 0.00727 \times L \qquad (18 \leq L \leq 21 \text{ and } T = 150\ ^{o}C) \qquad (4)$$

Where L (nm) is the mean crystal sizes and T is temperature. In addition, the 1D TiO_2 synthesized at 190°C further demonstrated that decreasing the crystal size from 58 to 21 nm

(increasing the BET SSA from 40 to 140 m^2 g^{-1}) was closely correlated with increasing the bandgap energy from 3.20±0.01 to 3.26±0.03 eV. The mean bandgap energy, E (ev), is

$$E = 3.307 - 0.00178 \times L \qquad (21 \leq L \leq 58 \text{ and } T = 190\ ^{o}C) \qquad (5)$$

Where L (nm) is the mean crystal sizes and T is temperature.

4. Conclusion

A statistical model was developed to evaluate the effects of the hydrothermal synthesis factors on the 1D TiO_2 bandgap energy. The AD statistic indicated an adequate fit of the statistical model to the experimental data. The model predicted optimized hydrothermal conditions for maximum and minimum bandgap energy. The temperature and NaOH concentration significantly affected the 1D TiO_2 bandgap energy, phase, crystal size and SSA, whereas the TiO_2 concentraction effect was negilible. The phase structure was the main reason for changes in bandgap energy. When compared to pure anatase, a decreasing bandgap energy trend was observed for the biphasic anatase-rutile and anatase-TiO_2-B structures. In addition, correlation between decreasing the crystal size (increasing the SSA) with increasing bandgap energy was due to the size quantization effect. The statistical model developed in this study can be used to guide the production of 1D TiO_2 with controllable bandgap energy, phase, mean crystal size and BET SSA.

Acknowledgements

Financial support for this work was provided by the Natural Sciences and Engineering Research Council (NSERC) of Canada (grant # 261797-2009) as well as the Ontario Trillium scholarship and the Canadian MITACS programs. We thank Dr. Bulent Mutus for assisting with

photoluminescence studies at the University of Windsor, Department of Chemistry and Biochemistry.

References

[1] A. Fujishima, K. Honda, Electrochemical photolysis of water at a semiconductor electrode, Nature. 238 (1972) 37–38. doi:10.1038/238037a0.

[2] B. O'Regan, M. Gratzel, A low-cost, high-efficiency solar cell based on dye-sensitized colloidal TiO_2 films, Nature. 353 (1991) 737–740. doi:10.1038/353737a0.

[3] J. Miao, R. Zhang, L. Zhang, Photocatalytic degradations of three dyes with different chemical structures using ball-milled TiO_2, Mater. Res. Bull. 97 (2018) 109–114. doi:10.1016/j.materresbull.2017.08.032.

[4] M. Stodolny, R. Zagrodnik, G. Nowaczyk, S. Jurga, Size-controlled synthesis of anatase nanobrush structures with higher crystal density, Mater. Res. Bull. 94 (2017) 335–341. doi:https://doi.org/10.1016/j.materresbull.2017.06.010.

[5] S. Malato, P. Fernández-Ibáñez, M.I. Maldonado, J. Blanco, W. Gernjak, Decontamination and disinfection of water by solar photocatalysis: Recent overview and trends, Catal. Today. 147 (2009) 1–59. doi:10.1016/j.cattod.2009.06.018.

[6] A. Di Paola, E. Garcia-Lopez, G. Marci, L. Palmisano, A survey of photocatalytic materials for environmental remediation, J. Hazard. Mater. 211-212 (2012) 3–29. doi:10.1016/j.jhazmat.2011.11.050.

[7] P. Roy, S. Berger, P. Schmuki, TiO_2 nanotubes: synthesis and applications, Angew. Chem. Int. Ed. 50 (2011) 2904–2939. doi:10.1002/anie.201001374.

[8] D.V. Bavykin, V.N. Parmon, A.A. Lapkin, F.C. Walsh, The effect of hydrothermal conditions on the mesoporous structure of TiO_2 nanotubes, J. Mater. Chem. 14 (2004) 3370–8. doi:10.1039/b406378c.

[9] H.Y. Zhu, Y. Lan, X.P. Gao, S.P. Ringer, Z.F. Zheng, D.Y. Song, et al., Phase transition between nanostructures of titanate and titanium dioxides via simple wet-chemical reactions, J. Am. Chem. Soc. 127 (2005) 6730–6736. doi:10.1021/ja044689.

[10] X. Chen, S.S. Mao, Titanium dioxide nanomaterials: Synthesis, properties, modifications, and applications, Chem. Rev. 107 (2007) 2891–2959.

[11] B. Chen, J. Hou, K. Lu, Formation mechanism of TiO_2 nanotubes and their applications in photoelectrochemical water splitting and supercapacitors, Langmuir. 29 (2013) 5911–5919. doi:10.1021/la400586r.

[12] T. Kasuga, M. Hiramatsu, A. Hoson, T. Sekino, K. Niihara, Formation of titanium oxide nanotube, Langmuir. 14 (1998) 3160–3163. doi:10.1021/la9713816.

[13] Y. Tang, Y. Zhang, J. Deng, J. Wei, H.L. Tam, B.K. Chandran, et al., Mechanical force-driven growth of elongated bending TiO_2-based nanotubular materials for ultrafast rechargeable lithium ion batteries, Adv. Mater. 26 (2014) 6111–6118. doi:10.1002/adma.201402000.

[14] H.Y. Zhu, Y. Lan, X.P. Gao, S.P. Ringer, Z.F. Zheng, D.Y. Song, et al., Phase transition between nanostructures of titanate and titanium dioxides via simple wet-chemical reactions, J. Am. Chem. Soc. 127 (2005) 6730–6736. doi:10.1021/ja044689.

[15] Y.V. Kolen'ko, K.A. Kovnir, A.I. Gavrilov, Hydrothermal synthesis and characterization of nanorods of various titanates and titanium dioxide, J. Phys. Chem. B. 110 (2006) 4030–4038. doi:10.1021/jp055687u.

[16] H.-W. Shim, D.K. Lee, I.S. Cho, K.S. Hong, D.-W. Kim, Facile hydrothermal synthesis of porous TiO_2 nanowire electrodes with high-rate capability for Li ion batteries, Nanotechnology. 21 (2010) 255706–9. doi:10.1088/0957-4484/21/25/255706.

[17] H.-L. Kuo, C.-Y. Kuo, C.-H. Liu, J.-H. Chao, C.-H. Lin, A highly active bi-crystalline photocatalyst consisting of TiO_2 (B) nanotube and anatase particle for producing H_2 gas from neat ethanol, Catal. Letters. 113 (2007) 7. doi:10.1007/s10562-006-9009-1.

[18] A.R. Armstrong, G. Armstrong, J. Canales, P.G. Bruce, TiO_2-B nanowires, Angew. Chem. 116 (2004) 2336–2338. doi:10.1002/ange.200353571.

[19] S. Preda, M. Rutar, P. Umek, M. Zaharescu, A study of thermal properties of sodium titanate nanotubes synthesized by microwave-assisted hydrothermal method, Mater. Res. Bull. 71 (2015) 98–105. doi:10.1016/j.materresbull.2015.07.015.

[20] D. Reyes-Coronado, G. Rodriguez-Gattorno, M.E. Espinosa-Pesqueira, C. Cab, R. de Coss, G. Oskam, Phase-pure TiO_2 nanoparticles: Anatase, brookite and rutile, Nanotechnology. 19 (2008) 145605. doi:10.1088/0957-4484/19/14/145605.

[21] I. Okura, M. Kaneko, Photocatalysis science and technology, Springer and Kodansha, Japan, 2002.

[22] S.D. Perera, R.G. Mariano, K. Vu, N. Nour, O. Seitz, Y. Chabal, et al., Hydrothermal synthesis of graphene-TiO_2 nanotube composites with enhanced photocatalytic activity, ACS Catal. 2 (2012) 949–956. doi:10.1021/cs200621c.

[23] R. Lopez, R. Gomez, Band-gap energy estimation from diffuse reflectance measurements on sol–gel and commercial TiO_2: a comparative study, J. Sol-Gel Sci. Technol. 61 (2012) 1–7.

[24] S. Ray, J.A. Lalman, N. Biswas, Using the Box-Benkhen technique to statistically model phenol photocatalytic degradation by titanium dioxide nanoparticles, Chem. Eng. J. 150 (2009) 15–24. doi:10.1016/j.cej.2008.11.039.

[25] S.R. Shanmugam, S.R. Chaganti, J.A. Lalman, D.D. Heath, Statistical optimization of conditions for minimum H_2 consumption in mixed anaerobic cultures: Effect on homoacetogenesis and methanogenesis, Int. J. Hydrogen Energy. 39 (2014) 15433–15445. doi:10.1016/j.ijhydene.2014.07.143.

[26] Y.Q. Wang, G.Q. Hu, X.F. Duan, H.L. Sun, Q.K. Xue, Microstructure and formation mechanism of titanium dioxide nanotubes, Chem. Phys. Lett. 365 (2002) 427–431. doi:10.1016/S0009-2614(02)01502-6.

[27] A. Chemseddine, T. Moritz, Nanostructuring titania: control over nanocrystal structure, size, shape, and organization, Eur. J. Inorg. Chem. 1999 (1999) 235. doi:10.1002/(sici)1099-0682(19990202)1999:2.

[28] J. Huang, Y. Cao, Q. Huang, H. He, Y. Liu, W. Guo, et al., High-temperature formation of titanate nanotubes and the transformation mechanism of nanotubes into nanowires, Cryst. Growth. Des. 9 (2009) 3632–3637. doi:10.1021/cg900381h.

[29] H. Luo, C. Wang, Y. Yan, Synthesis of mesostructured titania with controlled crystalline framework, Chem. Mater. 15 (2003) 3841–3846.

[30] H. Zhang, J.F. Banfield, Understanding polymorphic phase transformation behavior during growth of nanocrystalline aggregates: insights from TiO_2, J. Phys. Chem. B. 104 (2000) 3481–3487. doi:10.1021/jp000499j.

[31] S.S. Veeravalli, S.R. Chaganti, J.A. Lalman, D.D. Heath, Optimizing hydrogen production from a switchgrass steam exploded liquor using a mixed anaerobic culture in an upflow anaerobic sludge blanket reactor, Int. J. Hydrogen Energy. 39 (2014) 3160–3175. doi:10.1016/j.ijhydene.2013.12.057.

[32] Z. Lai, M. Zhu, X. Yang, J. Wang, S. Li, Optimization of key factors affecting hydrogen production from sugarcane bagasse by a thermophilic anaerobic pure culture, Biotechnol. Biofuels. 7 (2014) 131–11. doi:10.1186/s13068-014-0119-5.

[33] A. Reungsang, S. Pattra, S. Sittijunda, Optimization of key factors affecting methane production from acidic effluent coming from the sugarcane juice hydrogen fermentation process, Energies. 5 (2012) 4746–4757. doi:10.3390/en5114746.

[34] M.A. Stephens, EDF statistics for goodness of fit and some comparisons, J. Am. Stat. Soc. 69 (1974) 730–737. doi:10.1080/01621459.1974.10480196.

[35] H. Cheng, J. Ma, Z. Zhao, L. Qi, Hydrothermal preparation of uniform nanosize rutile and anatase particles, Chem. Mater. 7 (1995) 663–671. doi:10.1021/cm00052a010.

[36] T.P. Feist, P.K. Davies, The soft chemical synthesis of TiO_2 (B) from layered titanates, J. Solid State Chem. 101 (1992) 275–295. doi:10.1016/0022-4596(92)90184-W.

[37] M.C. Hidalgo, M. Maicu, J.A. Navío, G. Colón, Photocatalytic properties of surface modified platinised TiO_2: Effects of particle size and structural composition, Catal. Today. 129 (2007) 43–49.

[38] G. Tian, H. Fu, L. Jing, B. Xin, K. Pan, Preparation and characterization of stable biphase TiO_2 photocatalyst with high crystallinity, large surface area, and enhanced photoactivity, J. Phys. Chem. C. 112 (2008) 3083–3089. doi:10.1021/jp710283p.

[39] S.-D. Mo, W.Y. Ching, Electronic and optical properties of three phases of titanium dioxide: Rutile, anatase, and brookite, Phys. Rev. B. 51 (1995) 13023–13032. doi:10.1103/PhysRevB.51.13023.

[40] D. Yang, H. Liu, Z. Zheng, Y. Yuan, J.-C. Zhao, E.R. Waclawik, et al., An efficient photocatalyst structure: TiO_2(B) nanofibers with a shell of anatase nanocrystals, J. Am. Chem. Soc. 131 (2009) 17885–17893. doi:10.1021/ja906774k.

[41] D. Pan, N. Zhao, Q. Wang, S. Jiang, X. Ji, L. An, Facile Synthesis and Characterization of Luminescent TiO2 Nanocrystals, Adv. Mater. 17 (2005) 1991–1995. doi:10.1002/adma.200500479.

[42] B. Liu, L. Wen, X. Zhao, The photoluminescence spectroscopic study of anatase TiO_2 prepared by magnetron sputtering, Materials Chemistry and Physics. 106 (2007) 350–353. doi:10.1016/j.matchemphys.2007.06.012.

[43] J. Liqiang, S. Xiaojun, X. Baifu, W. Baiqi, C. Weimin, F. Honggang, The preparation and characterization of La doped TiO_2 nanoparticles and their photocatalytic activity, J. Solid State Chem. 177 (2004) 3375–3382. doi:10.1016/j.jssc.2004.05.064.

[44] H. Nakajima, T. Mori, Q. Shen, T. Toyoda, Photoluminescence study of mixtures of anatase and rutile TiO_2 nanoparticles: Influence of charge transfer between the nanoparticles on their photoluminescence excitation bands, Chem. Phys. Lett. 409 (2005) 81–84. doi:10.1016/j.cplett.2005.04.093.

[45] A. Monshi, M.R. Foroughi, M.R. Monshi, Modified Scherrer equation to estimate more accurately nano-crystallite size using XRD, World J. Nano Sci. Eng. 02 (2012) 154–160.

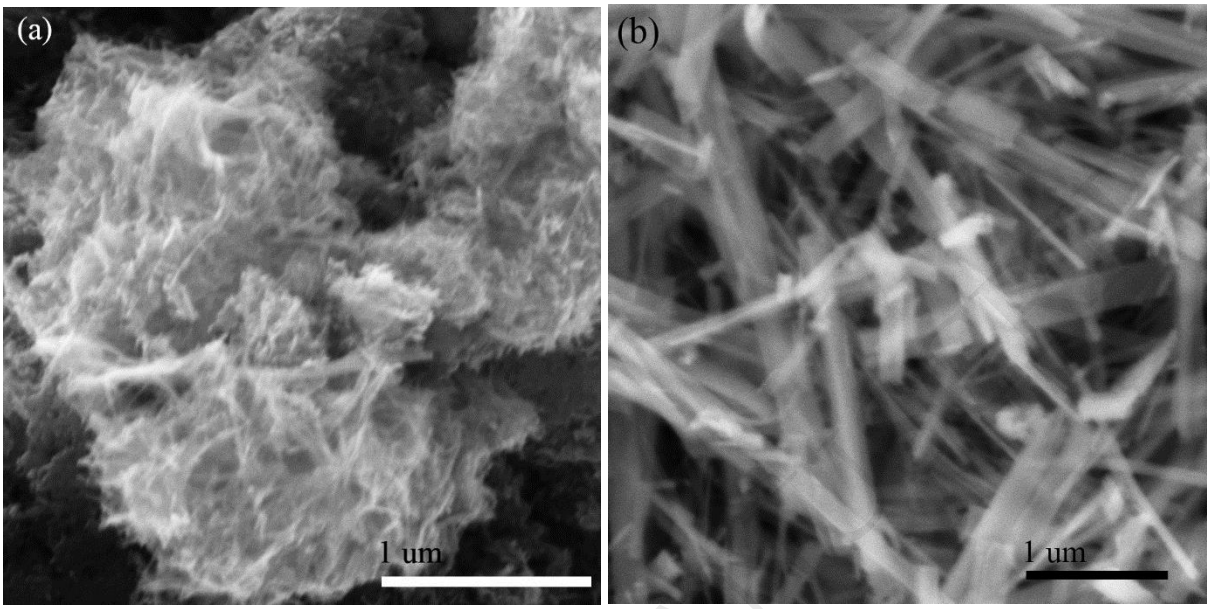

Figure 1: 1D TiO_2 SEM images for (a) sample #1 synthesized at 120°C, 5 M NaOH and 43 $g \cdot L^{-1}$ and (b) sample #6 synthesized at 190°C, 10 M and 14 $g \cdot L^{-1}$.

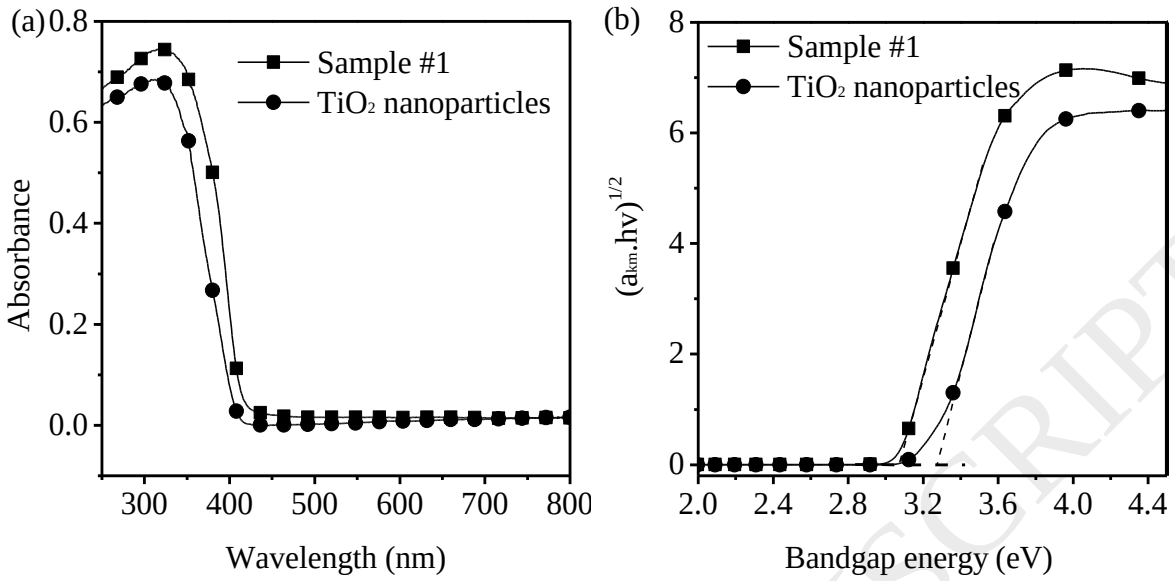

Figure 2: Diffuse reflectance UV-Visible spectroscopy and $a_{km}hv)^{1/2}$ versus absorbed energy profiles for Sample #1 (120ºC using 5 M NaOH and 43 $g \cdot L^{-1}$ TiO_2 nanoparticles) and TiO_2 nanoparticles. (a) Diffuse reflectance UV-Visible spectroscopy data (b) $a_{km}hv)^{1/2}$ versus absorbed energy profiles.

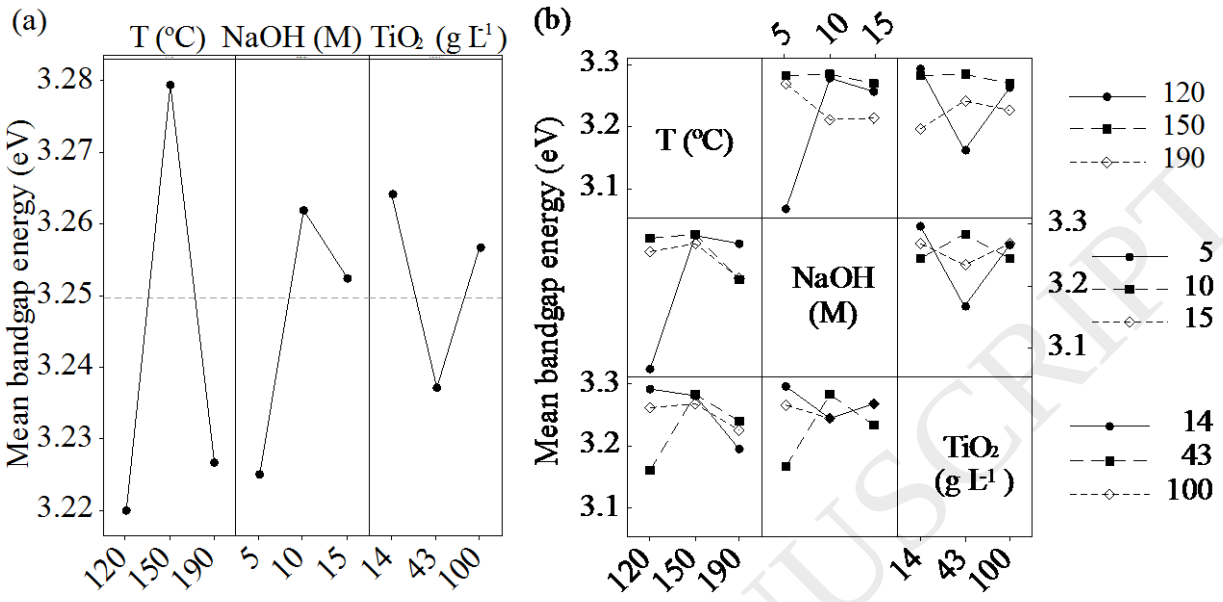

Figure 3: Three-level Box-Behnken design (BBD) plots for: (a) Main effects for bandgap energy and (b) Two-factor effects for bandgap energy.

Note: T, NaOH and TiO_2 represent temperature, NaOH concentration and TiO_2 concentration, respectively.

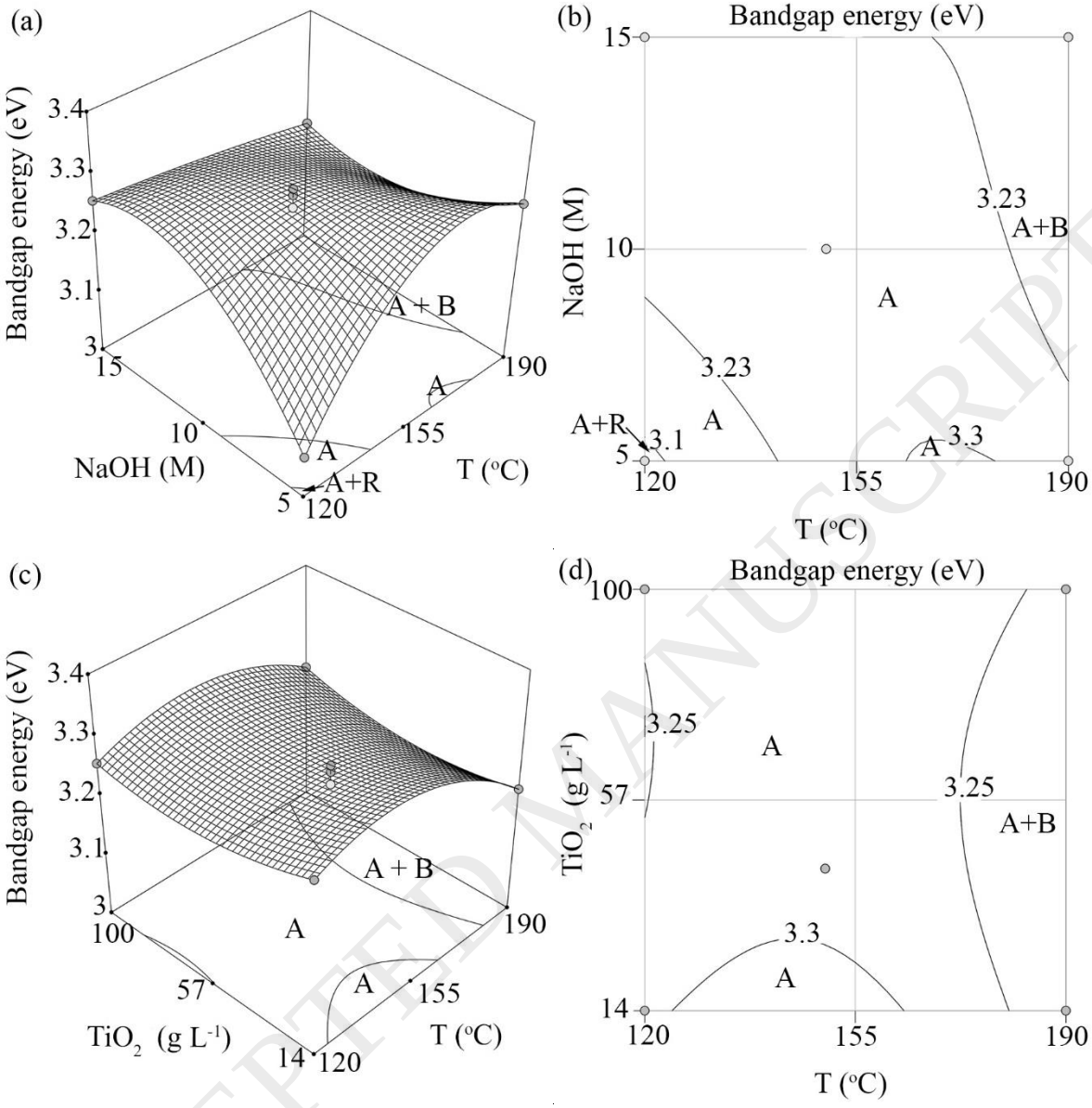

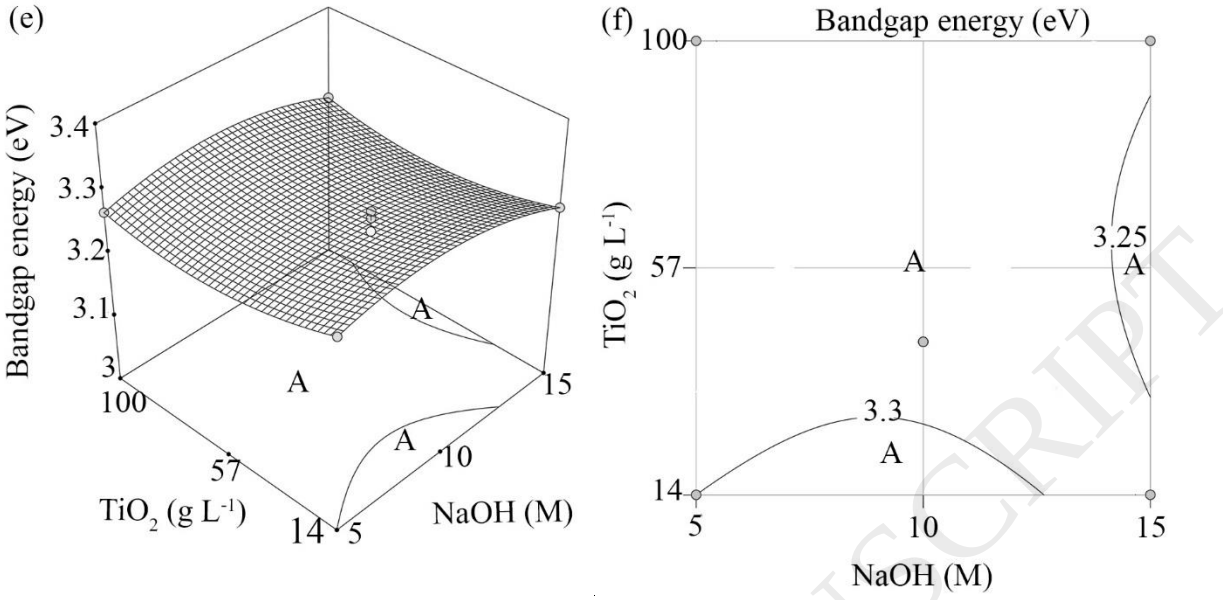

Figure 4: Bandgap energy response surface and contour plots for various factors: (a) and (b) Hydrothermal temperature and NaOH concentration with a TiO_2 concentration at 43 $g \cdot L^{-1}$; (c) and (d) Hydrothermal temperature and TiO_2 concentration with a NaOH concentration at 10 M; and (e) and (f) NaOH concentration and TiO_2 concentration with a temperature at 150^{o}C.

Note: A, R and B represent anatase, rutile and TiO_2-B, respectively.

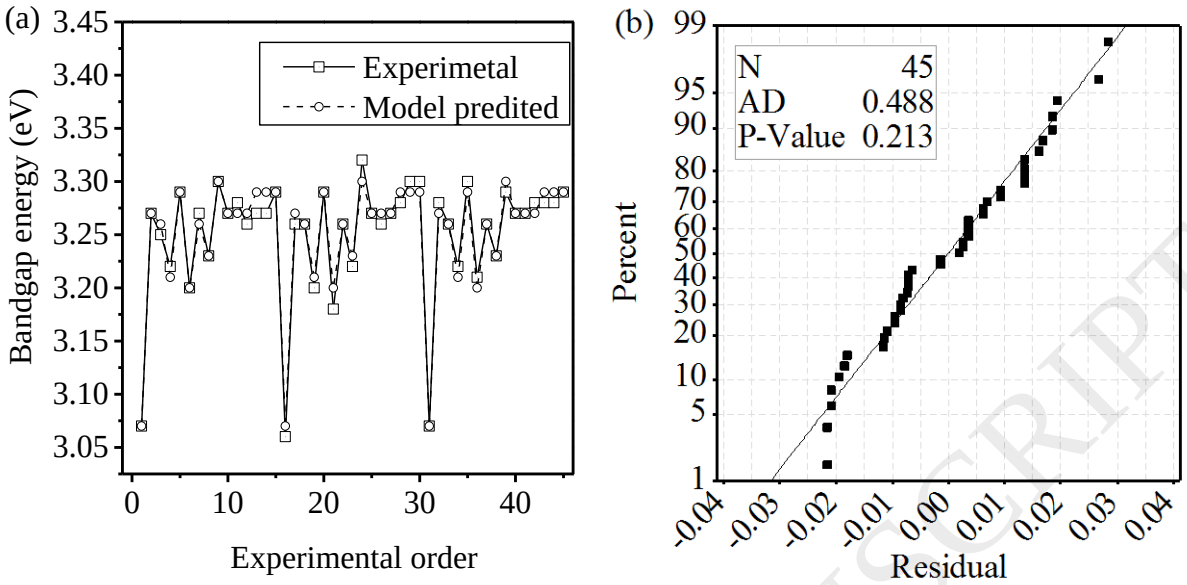

Figure 5: Evaluating the accuracy of the response surface model. (a) Scatter plot of the bandgap energy values versus the experimental order (45 experiments); (b) Anderson-Darling normality plot of residuals.

Notes: 1. N = the number of experiments that was conducted in this study; 2. P-Value = level of confidence; 3. AD = Anderson-Darling statistic.

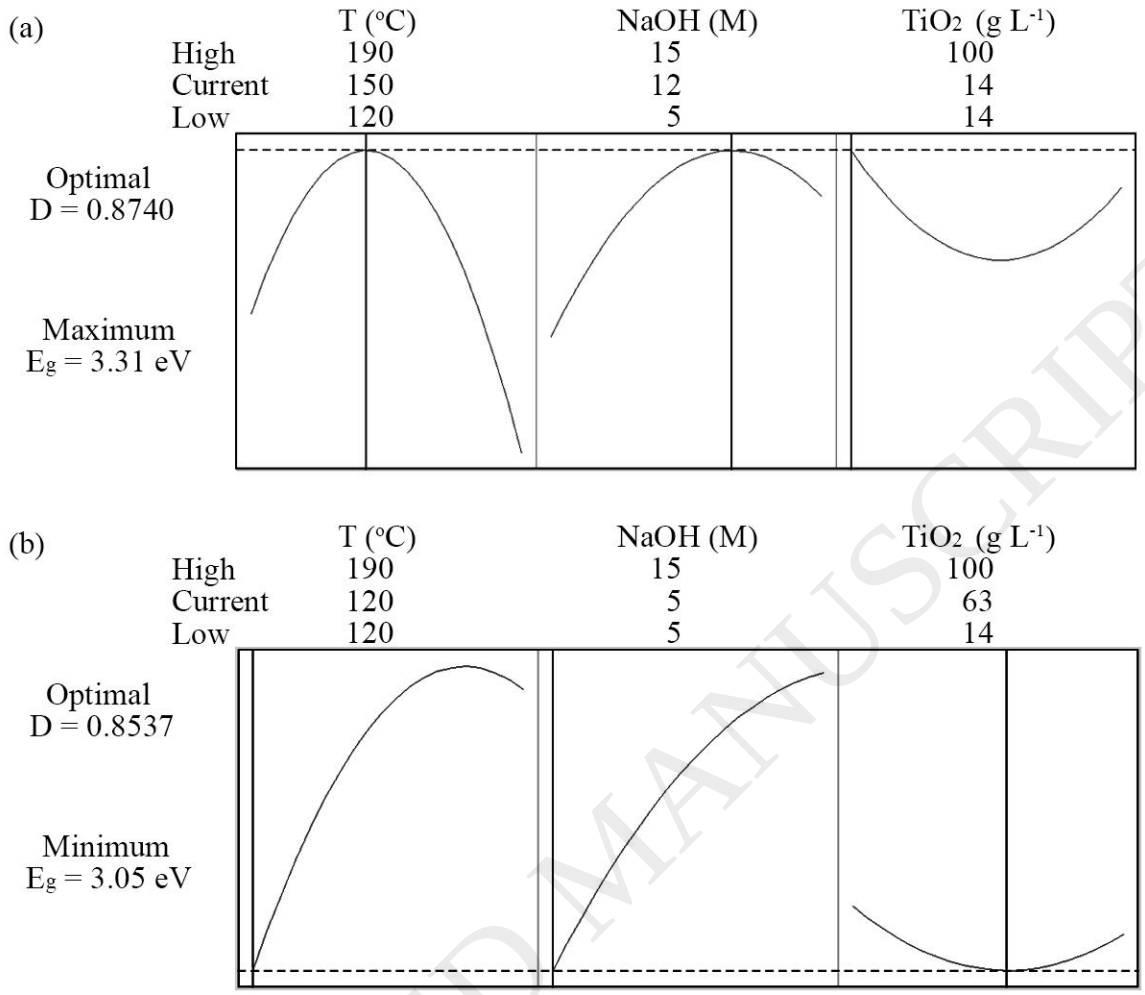

Figure 6: Optimality plot to locate optimum factor levels for (a) maximized response bandgap Eg and (b) minimized bandgap Eg.

(a)

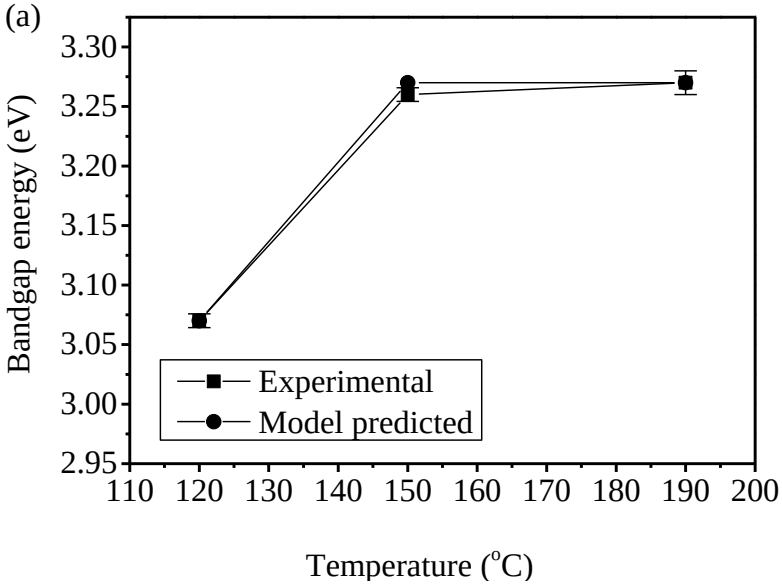

Temperature (^{o}C)

(b)

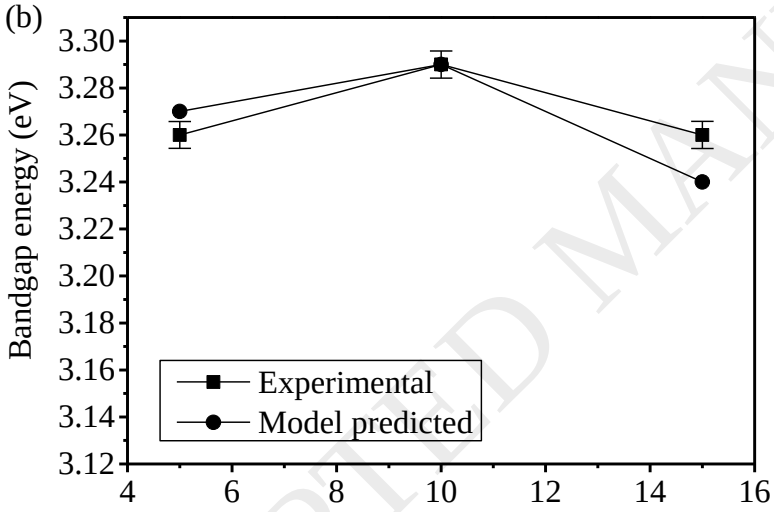

NaOH concentration (M)

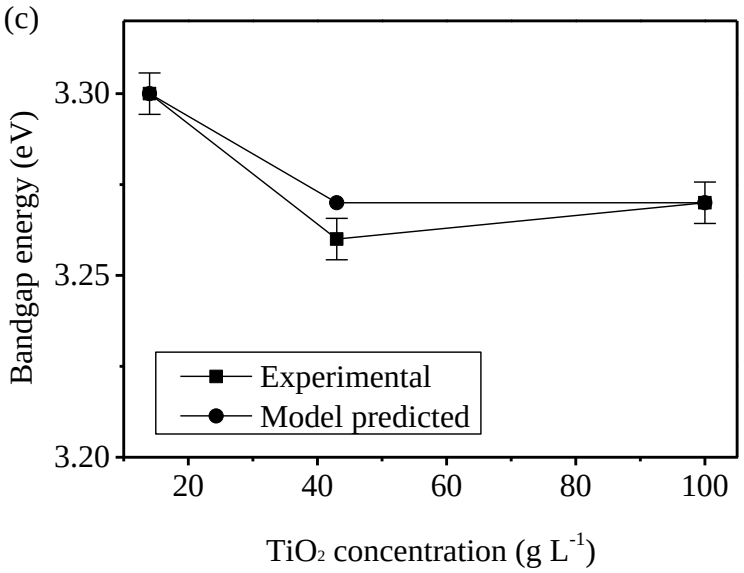

Figure 7: Validation study of the response surface model for the different factors under consideration. (a) Bandgap energy versus temperature at experimental condition set at 5 M NaOH and 43 g·L^{-1} TiO_2 concentration; (b) Bandgap energy versus NaOH concentration at experimental condition set at 150^{o}C and 43 g·L^{-1} TiO_2; (c) Bandgap energy versus TiO_2 mass at experimental condition set at 150^{o}C and 5 M NaOH.

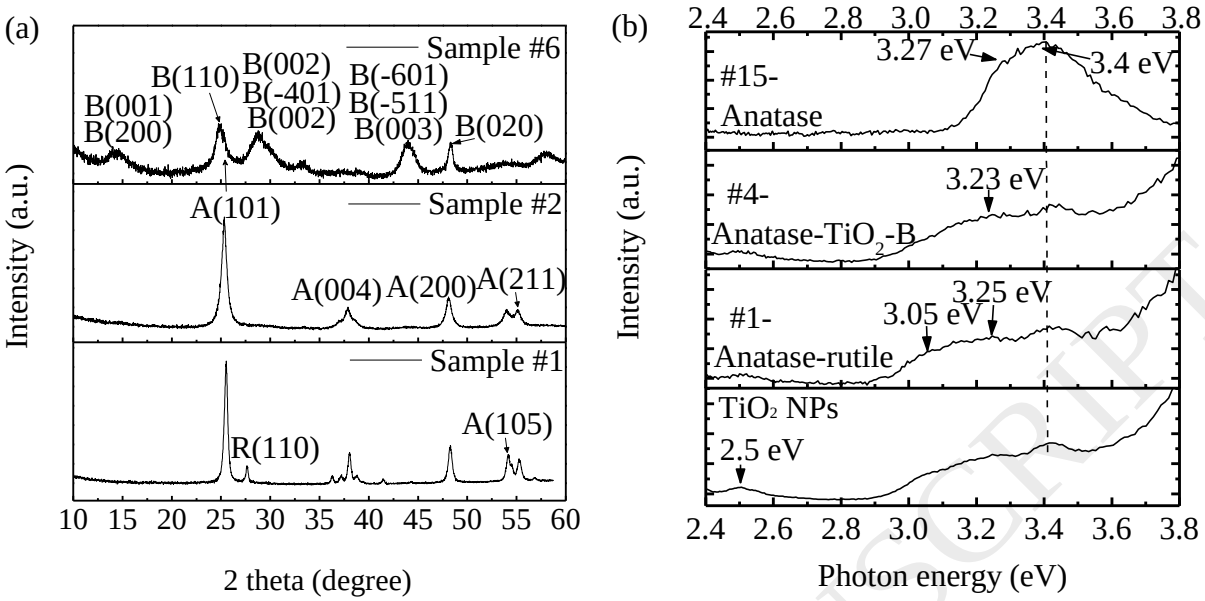

Figure 8: XRD and photoluminescence spectra for selected BBD samples. (a). XRD pattern for samples #1, #2, and #6, (b). Photoluminescence spectra for samples #1, #4, #15 and TiO_2 nanoparticles (NPs) excited at 300 nm (4.13 eV).

Notes: 1. Synthesis parameter details are listed in Table 2; 2. The A(101) peak is positioned on the shoulder; 3. A, R and B represent anatase, rutile and TiO_2-B, respectively.

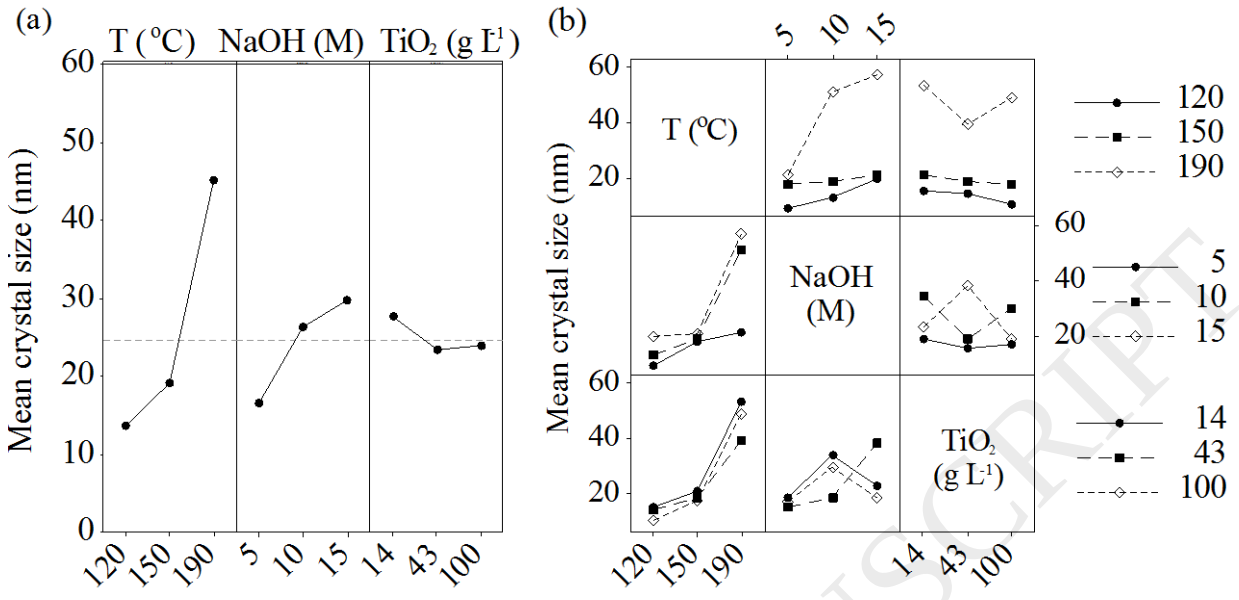

Figure 9: Main effects (a) and interaction (b) plots for mean crystal size (nm).

Note: T = temperature; NaOH = NaOH concentration and TiO_2 = TiO_2 concentration.

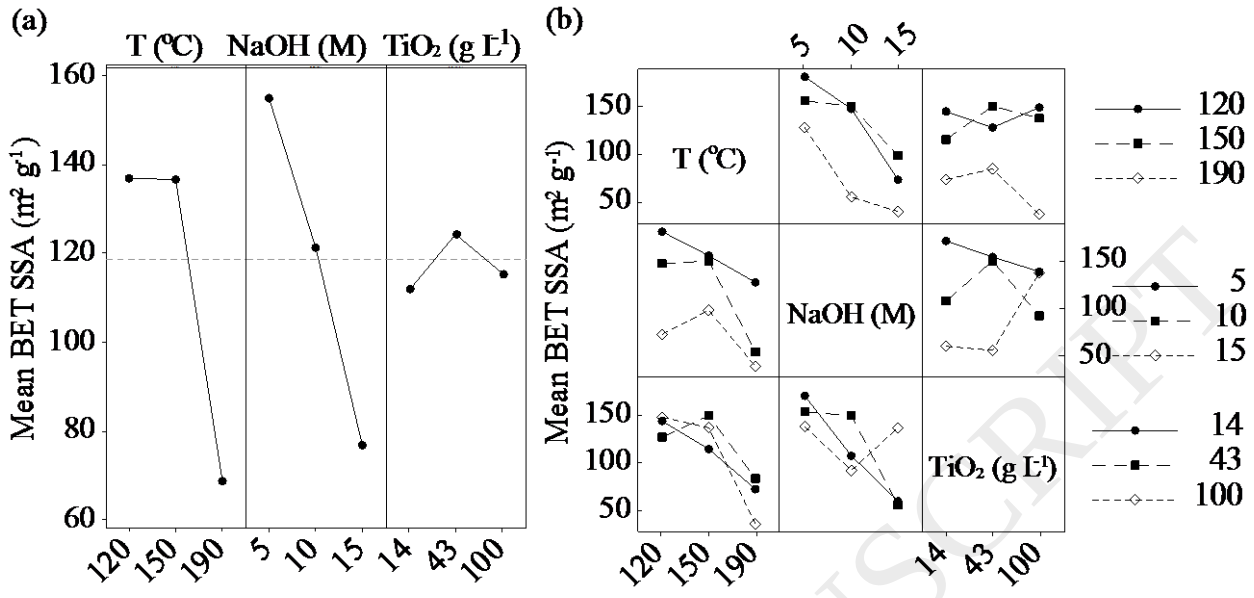

Figure 10: Main effects (a) and interaction (b) plots for mean BET SSA ($m^2 \cdot g^{-1}$).

Note: T = temperature; NaOH = NaOH concentration and TiO_2 = TiO_2 concentration.

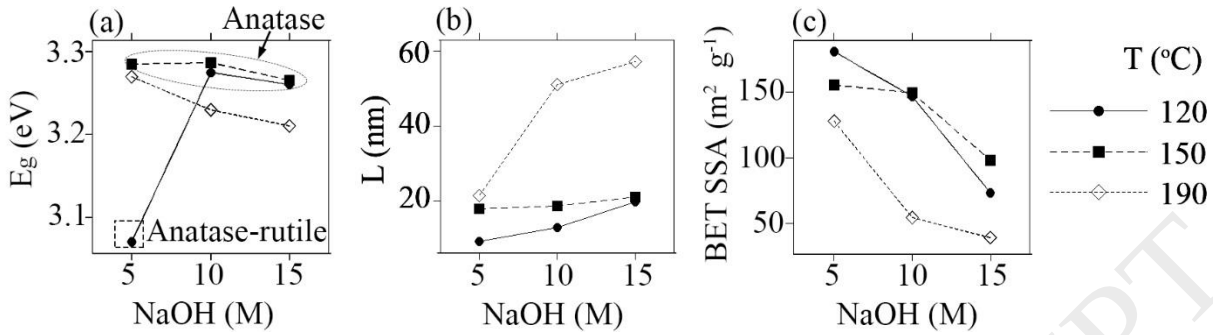

Figure 11: Interaction between temperature and NaOH concentration on (a) bandgap energy, (b) mean crystal size (L) and (c) BET SSA.

Note: 1. L, T and NaOH represent mean crystal size, temperature and NaOH concentration, respectively.

Table 1: Three selected factors and three levels.

Level	Factors		
	Temperature (°C)	**NaOH concentration (M)**	**TiO_2 concentration (g L^{-1})**
-1	120	5	14
0	150	10	43
1	190	15	100

Table 2: Design matrix for experimental factors and responses of bandgap energy Eg at different factor levels.

Expt. #	Factors			Bandgap energy E_g (eV)			
	T (°C) (X_1)	**NaOH (M) (X_2)**	**TiO_2 (g L^{-1}) (X_3)**	**E_{g1}**	**E_{g2}**	**E_{g3}**	**Mean±SD, E_g**
1	120	5	43	3.07	3.06	3.07	3.067±0.006
2	190	5	43	3.27	3.27	3.28	3.273±0.006
3	120	15	43	3.25	3.26	3.26	3.257±0.006
4	190	15	43	3.21	3.2	3.22	3.210±0.010
5	120	10	14	3.29	3.29	3.3	3.293±0.006
6	190	10	14	3.2	3.2	3.21	3.203±0.006
7	120	10	100	3.27	3.26	3.26	3.263±0.006
8	190	10	100	3.23	3.22	3.23	3.227±0.006
9	150	5	14	3.3	3.3	3.29	3.297±0.006
10	150	15	14	3.27	3.27	3.27	3.270±0.000
11	150	5	100	3.27	3.26	3.27	3.267±0.006
12	150	15	100	3.26	3.27	3.28	3.270±0.010
13	150	10	43	3.27	3.28	3.28	3.277±0.006
14	150	10	43	3.28	3.29	3.28	3.283±0.006
15	150	10	43	3.29	3.29	3.29	3.290±0.000

Notes:

1. Expt. # represents one experimental condition.

2. T, NaOH and TiO2 represents temperature, NaOH concentration and TiO2 concentration, respectively.
3. Eg represents bandgap energy. Eg1, Eg2 and Eg3 are replicates results for Eg
4. 4. SD = Standard deviation

Table 2: ANOVA results of the experimental response at each factor level.

Source	DF[1]	Seq. SS[2]	MS[3]	F-value	p-value
Model	9	0.09347	0.01039	6.97	0
X_1	1	0.00035	0.00035	0.23	0
X_2	1	0.00206	0.00206	1.39	0.001
X_3	1	0.00029	0.00029	0.2	0.62
X_1^2	1	0.03601	0.03601	24.18	0
X_2^2	1	0.00742	0.00742	4.98	0.146
X_3^2	3	0.00365	0.00365	2.45	0.255
X_1X_2	1	0.04115	0.04115	27.63	0
X_1X_3	1	0.00015	0.00015	0.1	0.046
X_2X_3	1	0.00001	0.00001	0	0.007
Error	35	0.05216	0.00008		
Total	44	0.14559			

Notes: 1. DF = degrees of freedom, 2. Seq. SS = sequential sum of square, 3. MS=mean square.

X1 = Temperature; X2 = NaOH concentration; X3 = TiO2 concentration.

Table 4: Phase structures and corresponding bandgap energies for all BBD samples

Sample #	Phase	Bandgap energy (eV)
2, 3, 5, 7 and 9-15	Anatase	3.26±0.01 - 3.297±0.005
1	Anatase and rutile	3.07±0.01
4, 6, 8	Anatase and TiO_2-B	3.20±0.01 - 3.23±0.01

Table 5: Design matrix for experimental factors and responses of mean crystal size and BET SSA at different factor levels.

Expt. #[a]	Factors[b]			Mean crystal size L (nm)	BET SSA (m^2 g^{-1})[c]
	T (°C) (X_1)	NaOH (M) (X_2)	TiO_2 (g L^{-1}) (X_3)		
1	120	5	43	9.3	181 ± 5
2	190	5	43	21.4	123 ± 5
3	120	15	43	19.8	73 ± 3
4	190	15	43	57.2	36 ± 3
5	120	10	14	18.2	145 ± 5
6	190	10	14	46.3	72 ± 3
7	120	10	100	16.6	149 ± 5
8	190	10	100	49.2	39 ± 3
9	150	5	14	18.9	172 ± 5
10	150	15	14	57.3	60 ± 3
11	150	5	100	21.1	139 ± 4
12	150	15	100	18.8	137 ± 5
13	150	10	43	19.5	150 ± 4
14	150	10	43	21.7	151 ± 5
15	150	10	43	17.8	148 ± 5

Notes: a Expt. # represents one experimental condition; b T, NaOH and TiO2 represents temperature, NaOH concentration and TiO2 concentration, respectively; crepresents the mean and standard deviation.